

Point Spread Function of real Wolter-I X-ray mirrors: computation by means of the Huygens-Fresnel principle

L. Raimondi^{1,2} and D. Spiga¹

¹INAF/ Osservatorio Astronomico di Brera, Via E. Bianchi 46, I-23807 Merate (LC), Italy

²Università degli Studi dell’Insubria, via Valleggio, 11, I-21100, Como, Italy

ABSTRACT

The Point Spread Function (PSF) of an imaging X-ray telescope is mostly determined by the defects of its grazing reflection optics. In terms of Fourier components of the mirrors’ profile, figure errors comprise long spatial wavelengths, whilst short spatial wavelengths are identified as microroughness. The former contribution is in general treated by means of geometrical optics, while the contribution of the latter – strongly dependent on the X-ray energy – is usually derived from the first order scattering theory. This approach, however, requires setting a sudden transition between these two treatments, whereas in the general case the change is expectedly more gradual. In order to compute the PSF expected from a mirror profile, we need a general method that does not need to classify surface defects as roughness or profile errors. In this work we show how to compute the PSF of real X-ray mirror shells in a typical Wolter-I configuration, at any X-ray energy. The suggested method is an application of the Huygens-Fresnel principle to grazing incidence Wolter-I profiles, and is an extension of the single-reflection formalism we presented in a previous paper. A few integral equations, applied from UV to hard X-rays, return the expected PSFs from measured or simulated profiles, accounting for the surface roughness along with its PSD (Power Spectral Density). The results are consistent with the ray-tracing results whenever geometric optic can be applied, and they merge with the results of the first order X-ray scattering theory when the roughness is within the smooth-surface limit. Finally, the PSF computed from the profile and the roughness of a real mirror is in very good agreement with the one experimentally measured in hard X-rays.

Keywords: X-ray mirrors, Point Spread Function, Wolter-I, Huygens-Fresnel principle

1. INTRODUCTION

Optics for imaging X-ray telescopes consist of a variable number of nested grazing-incidence, double-reflection X-ray mirrors. Most telescopes launched so far have adopted the Wolter-I profile, obtained by joining a grazing incidence parabolic mirror segment and a hyperbolic one.¹ The focusing occurs by two consecutive reflections onto these two surfaces. Alternative solutions can be envisaged, like polynomial profiles^{2,3} to enlarge the optic field of view, or Kirkpatrick-Baez⁴ geometries, but all solutions rely on two or more reflections. In addition to the intrinsic aberrations of the optical design, especially off-axis, it is the mirror quality that determines the concentration and imaging performances. These are commonly expressed in X-ray astronomy using the *Point Spread Function* (PSF), i.e., the annular integral of the focused X-ray intensity around the center of the focal spot. Another quantity of frequent use to denote the imaging properties is the *Half Energy Width* (HEW), i.e., twice the median value of the PSF. Achieving optical systems with high angular resolution (e.g., a 5 arcsec HEW for IXO) entails accurate mirror metrology over a wide range of spatial scales and methods to predict the PSF from metrology data.

Mirror imperfections affecting the PSF in X-rays are traditionally divided into “figure errors”, measured e.g., with optical profilometers, and “microroughness”, which can be measured with techniques like Phase Shift Interferometry or Atomic Force Microscopy. Excepting definitions empirically referred to the mirror length,⁵ the separation of profile geometry and roughness reflects in general the different treatment aimed at predicting their effect on the angular resolution. In terms of Fourier components, profile errors cover the long spatial scale range, where *geometric optics* can be applied. According to this definition, the profile PSF can be predicted by ray-tracing routines that unambiguously reconstruct the path of rays reflected at different mirror locations, regardless of the X-ray wavelength, λ . This method can be readily extended to multiple reflection systems, like the Wolter’s. In contrast, the surface roughness is assumed to entirely fall in a spectral region of spatial

wavelengths where the concept of “ray” is no longer applicable, because the optical path differences involved start to be comparable with λ . In this spectral range, the PSF broadening stems from the wavefront diffraction off the reflecting surface, or X-ray scattering (XRS), in general increasing with the X-ray energy. A well-established first order theory is available⁶ to compute the scattering diagram from the power spectrum of the roughness, also known as *Power Spectral Density*⁷ (PSD).

Different approaches were proposed^{5,8,9,10} to evaluate the impact of the XRS on the PSF, or to analytically translate¹¹ the surface PSD into the XRS contribution to the HEW, and vice versa, based on the known XRS theory. A problem arises, however, when the PSFs or the HEW values, separately obtained from geometry and scattering, have to be combined together. For example, the figure and scattering HEWs were believed to combine quadratically as long as figure and roughness are statistically independent,¹¹ but this assumption cannot be verified easily. Moreover, the separate treatment of geometry and XRS postulates a sudden transition. Such a boundary was identified by Aschenbach¹² by stating that the any *single* Fourier component whose rms, σ_n , fulfills the *smooth-surface condition*

$$4\pi\sigma_n \sin \alpha < \lambda, \quad (1)$$

where α is the grazing incidence angle of X-rays, should be classified as roughness. Fourier components exceeding this limit should instead contribute to the geometric errors. Although reasonable, this criterion can apparently be applied only to a discrete power spectrum. In addition, it seems more likely that the transition is more gradual, passing by a “mid-frequency” regime (often identified with the millimeter range of spatial wavelengths) where the application of either theory is uncertain. In other words, figure and XRS represent two *asymptotic* situations, applicable when the inequality in Eq. 1 is fulfilled (or not) in the sense of “much smaller” or “much larger”. The problem of bridging the figure error and the roughness was faced by Harvey et al.,¹³ but still distinguishing different spectral regimes and connecting the PSFs retrieved from each separate calculation. Despite these contributions, they did not provide yet a self-consistent method to compute the PSF, i.e., *a single formula to be applied to surface defects at any spatial scale, at any energy of the incident radiation*. This would reduce the roughness/figure dichotomy to a definition barely related to the measurement method.

In a previous SPIE volume¹⁴ we have provided a first solution. We have applied the Huygens-Fresnel principle in mono-dimensional approximation, proving that we can predict the PSF – and consequently the HEW – of a single, grazing incidence parabolic X-ray mirror from measured or simulated longitudinal profiles. This can be done at any energy, and regardless of the involved spatial frequencies, because the validity of the Huygens-Fresnel principle is unrestricted. Even though this principle is already used in wavefront propagation techniques, the sampling needed to include the high-frequency microroughness – that plays a major role in degrading the hard X-ray PSF – would imply an overwhelming time for computation, if performed over a two-dimensional surface. However, in grazing incidence the PSF calculation can be easily reduced to a monodimensional formalism, making the computation viable from UV light to hard X-rays, always using the same formula (Eq. 3).

We point out that a similar approach had already been suggested in 2003 by Zhao and Van Speybroeck,¹⁵ but apparently restricting the method, in Fraunhofer approximation, to the sole XRS computation. On the other side, Mieremet and Beijersbergen seem to have used it for the sole estimation of the aperture diffraction in the case of a pore optic.¹⁶ Our work is a generalization of their method, but it can be applied to simultaneously treat aperture diffraction, figure errors and roughness. In particular, the results merge with ray-tracing or the first order XRS results whenever they can be definitely applied.

In this paper we take a step forward. We present the extension of this method to an optical system with two grazing incidence reflections, and in particular applied to the Wolter-I geometry. The results obtained for single reflection mirrors are reviewed in Sect. 2. In Sect. 3 we show how to extend the Fresnel diffraction technique to a Wolter-I profile. In Sect. 4 we show some applications to a Wolter-I mirror including profile errors and roughness, from UV to hard X-rays, comparing the results to the corresponding PSFs for the parabolic (singly-reflecting) segment. In Sect. 5 we compare the HEW trends obtained from the Fresnel diffraction with the results of the analytical computation¹¹ if a “figure error” spectral regime can be easily recognized: in the considered case, characterized by a very low level of roughness in the millimeter range, the HEW trend from Fresnel diffraction matches very well the analytical approach results, provided that the figure HEW and the scattering HEW terms are *added linearly*, in accord with our previous findings for single-reflection mirrors,¹⁴ not in quadrature as initially supposed.¹¹ We also mention the results of the X-ray measurements performed at the Spring-8 radiation

facility¹⁷ with an optical module prototype for the NHXM optics:¹⁸ *the experimental hard X-ray PSFs are very well reproduced by applying the Fresnel diffraction theory to the measured profiles and roughness of the tested mirror.* This demonstrates not only the correctness of the adopted approach, but also its capabilities to predict the PSF at any energy from metrology data.

2. REVIEW OF RESULTS FOR SINGLE REFLECTION MIRRORS

In this section we review the application of the Fresnel diffraction theory to single reflection mirrors.¹⁴ The grazing incidence allows us working in scalar approximation and, if roundness errors can be neglected, using monodimensional profiles instead of the entire mirror surface. Consider thereby a grazing incidence mirror, with the axis oriented as the z -axis (Fig. 1), and have the image formed at $z = 0$, at a distance f from the mirror exit. Let the mirror be completely described by its axial profile of length L in the xz -plane, specified by the function $x_p(z_p)$. A planar wavefront of electric field amplitude E_0 impinges the profile along the z -axis from an infinite distance, at a nearly-constant incidence angle off-surface α . The mirror linear aperture, i.e., the difference of the maximum radius R_M and the minimum radius R_0 , has therefore the expression $\Delta R = L \sin \alpha$.

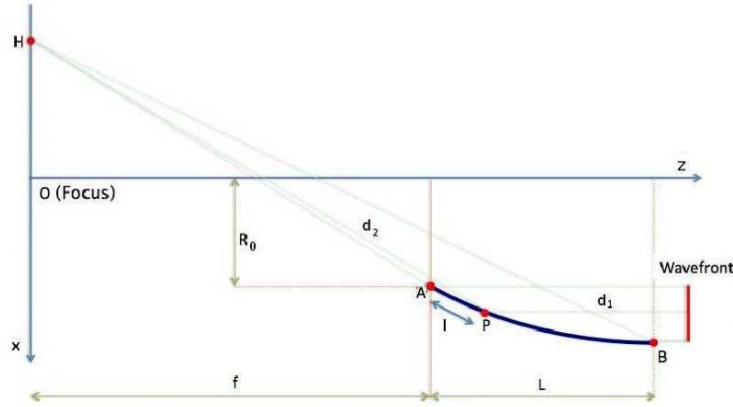


Figure 1. The adopted geometry for the computation of the PSF of a single parabolic mirror. The scattered amplitude at the generic point H of the focal plane is obtained by superposing the secondary waves generated at each point of the mirror profile, P, located by the curvilinear abscissa l .

The diffracted field at $z = 0$ has the expression

$$E(x, y) = \int_S \frac{E_0}{d_2 \lambda} \exp \left[-2i\pi \frac{d_1 + d_2}{\lambda} \right] d^2 s_{\perp}, \quad (2)$$

with $d^2 s_{\perp} = dl dy_p \sin \alpha$ is the diffracting area element; d_1 and d_2 are the distances of the generic mirror point from the initial wavefront, and from the focal plane point at x , respectively. The integral is computed over a mirror slice, S , of small amplitude $\Delta y \gg \lambda$ in the azimuthal direction. Because of the shallow incidence angles, f is much larger than the linear dimension of the mirror, which allows us performing the integrations over y_p and y quite easily. After some passages¹⁴ we find that the PSF can be described by the general formula:

$$PSF(x) = \frac{\Delta R}{f \lambda L^2} \left| \int_L e^{-i \frac{2\pi}{\lambda} (\sqrt{(x-x_p)^2 + z_p^2} - z_p)} dl \right|^2. \quad (3)$$

It is worth noting that the corresponding expression in the previous paper¹⁴ was derived omitting a factor of $(\Delta R/L)^2$ by mistake, that did not alter the subsequent results excepting for the absolute normalization ($1/\sin^2 \alpha$ instead of 1) of the simulated PSFs. Equation 3, in contrast, is correctly normalized to 1. If all coordinates are measured in mm, the PSF is in mm^{-1} . If one wants the x -axis graded in arcsec, it is sufficient to multiply the x -axis times the plate-scale factor $2.06 \times 10^5 / f(\text{mm})$ and to divide the PSF by the same factor.

We check the correctness of Eq. 3 in the case of a perfect parabolic mirror with focus in the origin of the reference frame, $z_p = ax_p^2 - \frac{1}{4a}$, where a is a parameter describing the aperture of the parabolic profile. After substitution and some manipulation, this yields

$$PSF(x) = \frac{\Delta R}{f\lambda L^2} \left| \int_L e^{-i\frac{2\pi}{\lambda}(\sqrt{x^2 - 2x_p x + (ax_p^2 + \frac{1}{4a})^2} - ax_p^2)} dl \right|^2; \quad (4)$$

an exact solution of this integral is possible only if $x = 0$. If $x \neq 0$, we notice that the image is much smaller than the mirror's size, i.e., $x \ll x_p$, therefore we can neglect x^2 with respect to $2x_p x$ in the exponent of the integrand of Eq. 4, and the square root can be developed at the first order. In this way, we remain with

$$PSF(x) \approx \frac{\Delta R}{f\lambda L^2} \left| \int_L e^{-i\frac{2\pi}{\lambda} \frac{x_p x}{z_p}} dl \right|^2. \quad (5)$$

Setting now $dl \approx dz_p \approx (L/\Delta R) dx_p$ and $z_p \approx f$ in the exponent denominator, the integral is easily computed:

$$PSF(x) \approx \frac{1}{f\lambda\Delta R} \left| \int_{R_0}^{R_0+\Delta R} e^{-i\frac{2\pi x}{\lambda f} x_p} dx_p \right|^2 = \frac{\beta \sin^2 \beta x}{\pi (\beta x)^2}, \quad (6)$$

where we set $\beta = \frac{\pi\Delta R}{f\lambda}$. This is the usual diffraction pattern from a slit of aperture ΔR , correctly normalized to 1: when $\Delta R \gg \lambda$ the PSF tends to a Dirac delta, as expected.

Excepting a few cases, the integral in Eq. 3 has to be computed numerically. This entails the issue of approximating the integral with a sum of sufficiently large number of terms. We already estimated¹⁴ the maximum frequency to be sampled to avoid the appearance of aliases. Even if the adopted profile sampling, Δl , already oversampled this maximum frequency by a factor of 2π , the sampling should be halved as per the Nyquist criterion:

$$\Delta l \approx \frac{\lambda f^2}{2\pi R_0 r}, \quad (7)$$

where r is the detector half-size. This sampling was derived assuming that the scattering at the detectors edge can be described by the 1st order theory, i.e., that the detector is sufficiently large to fit all the PSF associated to higher scattering orders, which blend to form the “figure error” PSF (also owing to the imperfect monochromaticity of the incident radiation). Actually, this condition is automatically fulfilled, because any scattering of the k^{th} ($k > 1$) order at the detector's edge would be generated by a spatial wavelength k times larger, which would be even more oversampled by the sampling of Eq. 7.

However, we did not specify yet the minimum required sampling on the focal plane in order to avoid undersampling of the PSF: this is obtained from the smallest spatial frequency visible on the mirror profile, $1/L$, resulting in a scattering at a distance Δx :

$$\Delta x \approx \frac{\lambda f^2}{\pi R_0 L}, \quad (8)$$

where we increased the sampling by a factor of 2π for consistency with Δl . We note that

$$\frac{L}{\Delta l} = \frac{2r}{\Delta x} := N, \quad (9)$$

i.e., N , the number of points on the mirror profile and on the detector line is the same. N increases linearly with the X-ray energy, but even assuming *very* hard X-rays of wavelength $\lambda = 0.1 \text{ \AA}$, $r = 2 \text{ cm}$, $f = 10 \text{ m}$, $R_0 = 150 \text{ mm}$, and $L = 300 \text{ mm}$ we obtain $N \approx 10^6$, a number of terms that can be managed quite easily. The total computation time increases as N^2 , i.e., with the square of the X-ray energy, E ,

$$\tau \propto \frac{E^2 R_0^2 r^2 L^2}{f^4}. \quad (10)$$

3. EXTENSION OF THE METHOD TO DOUBLE REFLECTION MIRRORS

3.1 Method generalization

We have hitherto considered the case of single reflection mirrors. However, it would be interesting to apply the previous formalism to an optical system with two consecutive reflections, like a Wolter-I. In principle, the electric field computation (Eq. 2) can be generalized to any mirror surface even if the incident wavefront is not planar,

$$E(x, y) = \int_S \frac{E_0(\underline{x}') e^{-i\xi(\underline{x}')} }{d_2 \lambda} \exp\left(-2i\pi \frac{d_2}{\lambda}\right) d^2 s_{\perp}, \quad (11)$$

where E_0 is the electric field amplitude at the coordinates \underline{x}' on the mirror and ξ its phase at the same position. The method to extend the PSF computation to a double reflection consists of computing the electric field amplitude and phase as diffracted by the first mirror, at the surface of the second one, using Eq. 2. The subsequent computation of the diffracted field at the focal plane is obtained via Eq. 11. Nevertheless, the reduction to a single integral (like in Eq. 3) is an important step, otherwise the complexity of the computation will be overwhelmingly increased. Now, Eq. 3 is derived assuming that *the distance to the diffracting mirror is much larger than its linear dimensions* (“far field”). The reason is that some approximations are needed¹⁴ to enable the fast integration over the y_p variable. If the mirrors are not separated by a large distance, like in the Wolter-I case (Sect. 3.2), the reduction to a single integration over the axial profile is more complicated, but still viable.

3.2 Application to a Wolter-I configuration

In a Wolter-I mirror shell, we cannot apply the far field approximation in the computation of the electric field on the hyperbolic profile, because the two segments intersect each other. For this reason, we cannot approximate $d_2 \approx f$ in the denominator of Eq. 2. Moreover, the funneling of rays toward the hyperbola owing to the azimuthal curvature is negligible at such a short distance, therefore the integration over the azimuthal coordinate is more complicated than in Fraunhofer approximation. Nevertheless, the integration is still feasible. We assume the two segments to have the same lengths, L , as measured *along the z-axis*, and f to be the distance of the intersection plane from the focal plane xy . We denote with R_0 the mirror radius at the focal plane, and with R_M the mirror radius at the shell entrance ($z_p = f + L$).

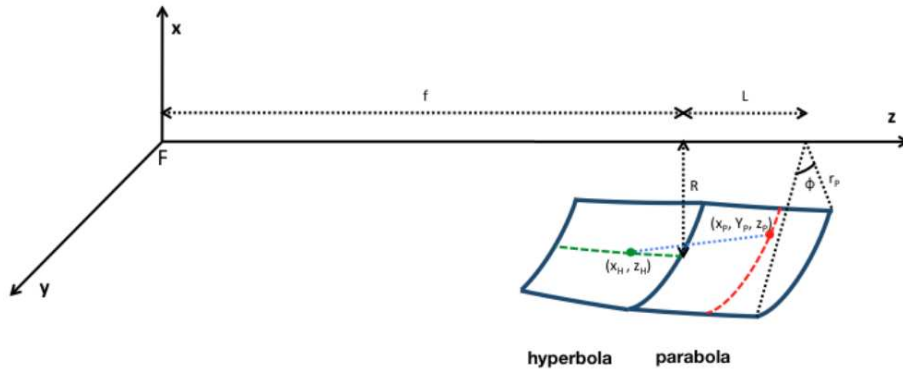


Figure 2. Scheme of a Wolter-I mirror. In this case we cannot apply the *far field* approximation in the computation of the electric field at the hyperbolic profile, therefore the integration over the azimuth has to be performed carefully.

The computation of the field at the hyperbolic profile (Fig. 2) at $y_h = 0$, (x_h, z_h) is performed along with Eq. 2, using the expressions of d_1 and d_2 , mapping the parabola in cylindrical coordinates (r_p, ϕ_p, z_p) ,

$$d_1 = f + L - z_p \quad (12)$$

$$d_2 = \sqrt{r_p^2 + x_h^2 + (z_p - z_h)^2 - 2x_h r_p \cos \phi_p}, \quad (13)$$

where $r_p = x_p$ in the xz plane because of the supposed axial symmetry. Assuming that $\lambda L \ll R_0^2$, an hypothesis in general fulfilled, we are allowed to simplify the exponent. Then, making use of Fresnel integrals, we can perform the integration over ϕ_p . The computation is too long to reproduce here, but this reduces the expression for the (complex) field at the hyperbolic surface to a simple integral in z_p :

$$E_h(x_h, z_h) = \frac{E_0 \Delta R}{L \sqrt{\lambda x_h}} \int_f^{f+L} \sqrt{\frac{x_p}{\bar{d}_2}} e^{-\frac{2\pi i}{\lambda}(\bar{d}_2 - z_p)} dz_p, \quad (14)$$

where $\Delta R = R_M - R_0$ (Sect. 2), we omitted an unessential phase factor and defined

$$\bar{d}_2 = \sqrt{(x_p - x_h)^2 + (z_p - z_h)^2}. \quad (15)$$

In Eqs. 14 and. 15 we have restored the x_p variable, replacing r_p .

The intensity of the electric field intensity on the hyperbolic profile exhibits the typical oscillations of the Fresnel diffraction pattern from a straight edge (Fig. 3). Moreover, note that the field is diffracted *beyond the hyperbola edge*, where the intensity is always nonzero: both oscillations and edge transition become more abrupt as λ decreases. All curves intersect at the edge of the region geometrically illuminated by the parabolic segment, where the intensity is – as expected from diffraction theory – $1/4$ of the incident one. This is slightly shorter than the hyperbola length, owing to the curvature of the axial profile: were it a double cone, the illumination edge would have exactly matched the edge of the hyperbola.

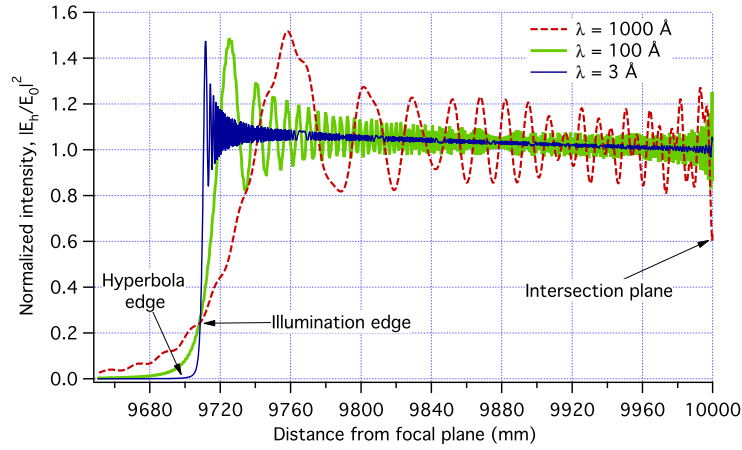


Figure 3. The field intensity along the hyperbolic profile in a perfect Wolter-I mirror, at $\lambda = 3000 \text{ \AA}$, 100 \AA , and 3 \AA , as computed with Eq. 14. We assumed that $L = 300 \text{ mm}$, $R_0 = 150 \text{ mm}$, and $f = 10 \text{ m}$.

The complex electric field E_h (Eq. 14) is then used to compute the field intensity on the focal line, this time in far field approximation and accounting for the power concentration owing to the azimuthal curvature.¹⁴ Then we obtain the normalized PSF by dividing the focused intensity by the incident flux,

$$PSF(x) = \frac{\Delta R}{E_0^2 f \lambda L^2} \left| \int_{f-L}^f E_h(x_h, z_h) e^{-i \frac{2\pi}{\lambda} (\sqrt{(x-x_h)^2 + z_h^2} - z_h)} dz_h \right|^2. \quad (16)$$

The PSF is independent of the incident radiation intensity and normalized to 1 when integrated over x .

In the remainder of this paper we make use of Eqs. 14 and 16 to simulate the PSFs of Wolter-I mirrors characterized by various profile errors and roughness. The numerical computation requires appropriate sampling of the parabolic profile, of the hyperbolic profile, and of the focal line: the optimal samplings can be established along with arguments analogous to those reported in Sect. 2, e.g., for the sampling on the parabola the angular acceptance of the detector shall be replaced with the one of the hyperbola, α . All the computed PSFs will behave according to the expectations.

4. EXAMPLES OF PSF COMPUTATION FOR WOLTER-I MIRRORS

4.1 Perfect Wolter-I mirrors

He hereafter consider as a test case a Wolter-I mirror shell with $f = 10$ m, $R_0 = 150$ mm, $L = 300$ mm, $\alpha = 0.21$ deg. The analytical expressions $x_p = x(z_p)$ and $x_h = x(z_h)$ of Wolter-I nominal profiles,¹ when substituted into Eqs. 14 and 16 return a sinc-shaped PSF (Fig. 4, left) that becomes more peaked and narrow as λ is decreased, as expected. In UV, the broadening caused by the aperture diffraction is clearly seen. It is worth pointing out that, even for a perfect Wolter-I mirror, the HEW in UV light is sensitively larger than the one resulting from a sole perfect parabolic segment, because the aperture diffraction occurs *twice*. Since many optical tests on Wolter-I X-ray mirrors are performed in UV light, the accurate subtraction of the diffraction aperture term should account also for the small difference introduced by the double reflection. In X-rays, the PSF resembles a Dirac delta function for both single and double reflection cases, as expected (Fig. 4, right).

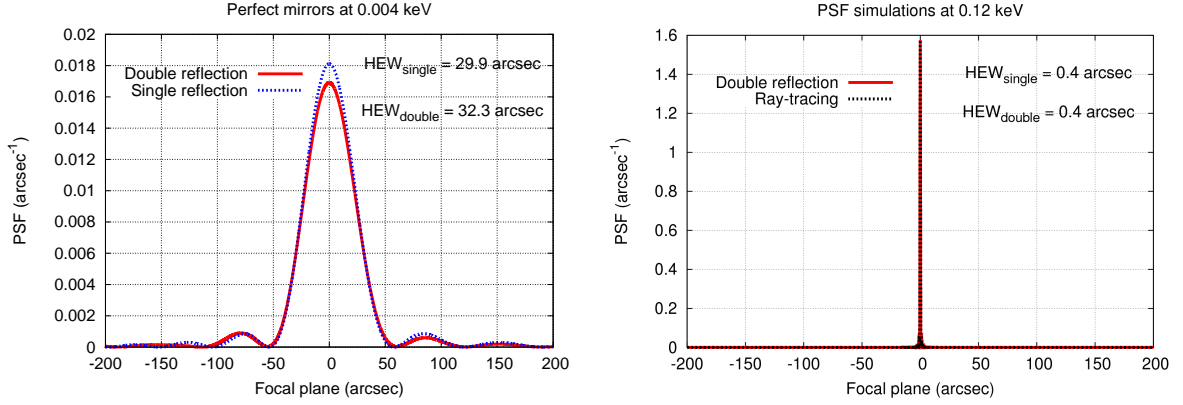


Figure 4. The PSFs of an ideal Wolter-I mirror. (left) in UV light at 3000 Å. (right) at 100 Å.

4.2 Sinusoidal grating on parabola, perfect hyperbola

As a first example of imperfect Wolter-I mirror (sized as in Sect. 4.1), we have considered a sinusoidal grating with 0.1 μ m of amplitude and 10 cm of period, *on the sole parabolic profile* (Fig. 5, left). This case was already treated extensively for the case of a single reflection mirror,¹⁴ finding that the same grating may behave according to the 1st order XRS theory, exhibit higher interference orders, or even comply the geometrical optics, depending on the X-ray wavelength in use. In particular at 0.4 keV, an energy that slightly exceeds the smooth surface limit (Eq. 1), we find that higher orders appear, but the grating is far from behaving according to geometrical optics.

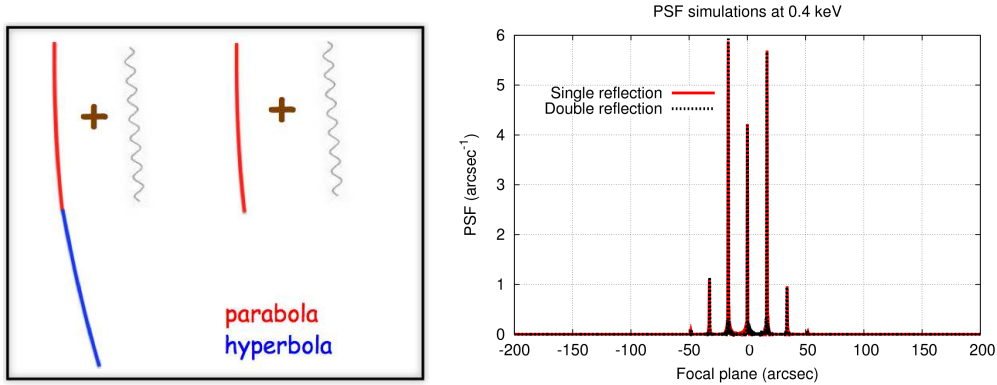


Figure 5. (left) Scheme of a Wolter-I profile with a sinusoidal grating (period 1 cm, amplitude 1 μ m) on the sole parabola, Vs. a single reflection parabolic mirror with the same defect and the same size as the one of the Wolter's. (right) At 30 Å, the PSF simulation for the Wolter-I mirror with the perturbed parabolic profile returns exactly the same result as the single reflection case. The first orders are still dominant, but the second order peaks are already visible.

Now, since the hyperbola profile is not perturbed and aperture diffraction effects are negligible at 0.4 keV, we expect that the beam diffracted by the grating is simply reflected to the focal plane preserving the intensity distribution. In fact, the simulated PSF is very well superposed to the one of the parabolic profile with the same incidence angle and grating (Fig. 5, right). This example puts Eq. 14 to the test: if the calculation were inaccurate, the subsequent diffraction would not have reproduced the exact positions and heights of the single reflection peaks, which – as a further confirmation – correspond exactly to those predicted by the sinusoidal grating theory. The same result is obtained imparting the sinusoidal profile to the sole hyperbola.

4.3 Long-period deformations of parabola and hyperbola

As a second example, we take into account a deformation on both mirror segments. Aiming at checking the validity and the accuracy of Eqs. 14 and 16, we have considered a profile whose effects are easily predictable in an independent fashion, e.g., along with a ray-tracing code. From the previous discussion (Sect. 1) we can expect that a single deformation with a long period, i.e., comparable to a 300 mm mirror length, should be treated with geometrical optics at, e.g., 0.1 keV. We have superposed the following perturbation to the segments of the Wolter-I mirror:

$$x_p(z_p) = \pm \frac{Lw}{4\beta} \log \cos \left(\frac{\beta z_p}{L} \right), \text{ with } \beta \lesssim \pi, \quad (17)$$

where w is the Half Energy Width for a single reflection, measured in radians, and β must be slightly less than π to avert a profile divergence. This figure error is tailored to return a Lorentzian-shaped PSF (a particular case of the well-known King function), as long as the aperture diffraction is negligible:

$$PSF(\theta) = \frac{2w}{\pi(w^2 + 4\theta^2)}, \quad (18)$$

where $\theta = x/f$, in radians. This PSF is a realistic model, e.g., SWIFT-XRT's matches very well a King shape:¹⁹ on the other hand, Eq. 17 is the simplest profile, though not the only one, to be consistent with such a PSF. Since the $x_p(z_p)$ profile can be taken with either sign, we have added the profile in Eq. 17 to the two segments with either the same sign or opposite signs. We have then computed the PSFs applying Eqs. 14 and 16.

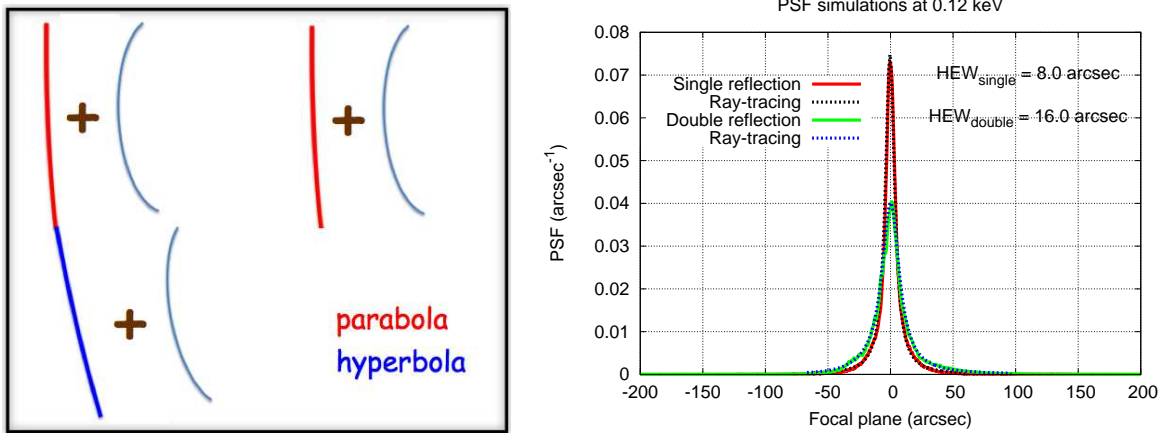


Figure 6. The PSF of a Wolter-I mirror with the same figure error (Eq. 17) at 100 Å, assuming $L = 300$ mm and $w = 8$ arcsec. Also plotted for comparison is the PSF simulated from the single reflection. The results match the ray-tracing prediction accurately (dots).

If the two deformations have the same sign, the PSF spread is amplified (Fig. 6) with respect to the single reflection case. More exactly, the HEW of the Wolter-I deformed mirror equals 16 arcsec, exactly twice the HEW in single reflection. In contrast, if the two errors have opposite signs (Fig. 7), the angular deviations are expected to compensate each other: in fact, the PSF computation correctly returns a nearly perfect delta function, with a HEW close to zero. All results are in perfect agreement with the results of the ray-tracing routine (definitely applicable in these cases). It is worth noting that these results contradict the common belief that the PSF of the Wolter-I mirror is the convolution of the PSFs of the two segments.

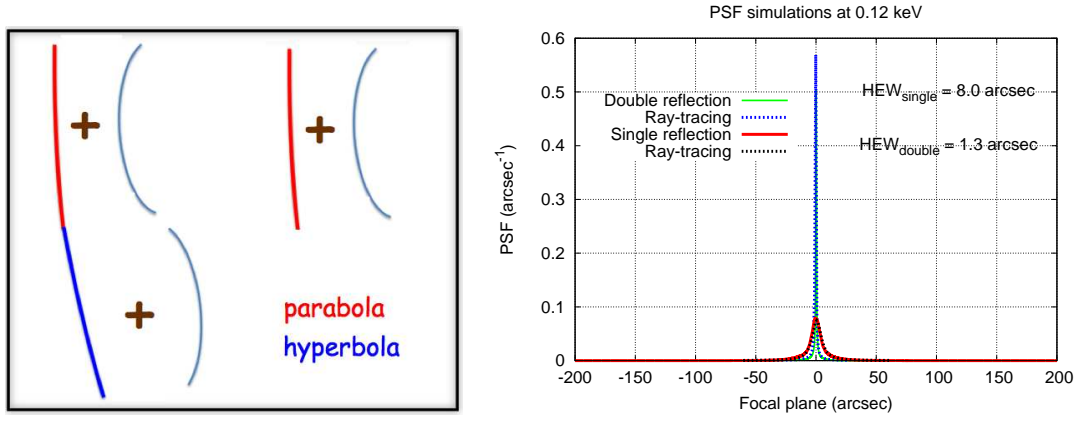


Figure 7. The PSF of a Wolter-I mirror with opposite figure error (Eq. 17) at 100 \AA , assuming $L = 300 \text{ mm}$ and $w = 8 \text{ arcsec}$. Also plotted for comparison is the PSF simulated from the single reflection. The results match exactly the ray-tracing prediction (dots)

4.4 Parabola and hyperbola with long-period deformations and roughness

As a last example, we consider a more realistic case accounting for both figure errors and roughness, as we already did for the single reflection.¹⁴ We have adopted the mirror dimensions as in Sect. 4.1 and as figure error the same profile of Eq. 17 for both mirror segments (Fig. 6). The roughness is described by a Power Spectral Density (PSD) expressed by a power-law function,²⁰ $P(f) = K_n/f^n$, where the spectral index n and the coefficient K_n depend on the surface finishing level. We have assumed as realistic parameter values $n = 1.8$ and $K_n = 2.2 \text{ nm}^3 \mu\text{m}^{-1.8}$, and we have generated two of the infinitely possible profiles from this power spectrum. After superposing the rough profiles to the modeled figure errors and selecting a value for λ , we have computed the expected PSF using Eqs. 14 and 16. To reduce the noise in the PSF resulting from the pseudorandom nature of roughness, we have repeated the computation a few times and averaged the results. The average is needed only in hard X-rays, where the roughness effect starts to become apparent. Finally, the PSF has been degraded to a realistic spatial resolution of the detector ($20 \mu\text{m}$). The computation has been performed at several wavelengths from ultraviolet light to hard X-rays, always applying the same equations. The resulting PSFs are reported in Figs. 8 through 12, for increasing energies. We note that the aperture diffraction gradually disappears and the mirror deformation effects become visible. For $\lambda < 10 \text{ \AA}$, the effect of roughness causes the PSF to broaden and the HEW to consequently increase (see also Sect. 5).

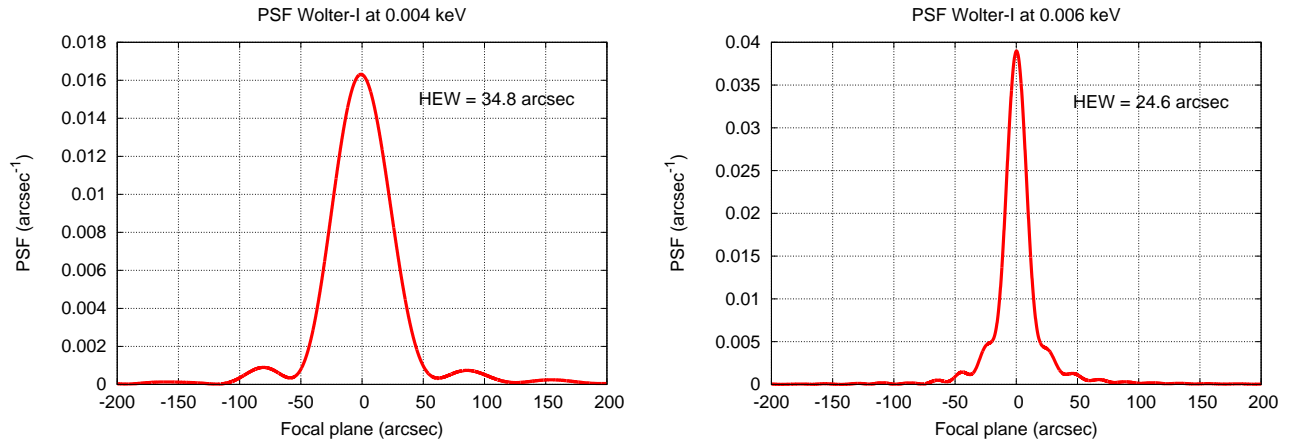


Figure 8. The simulated PSF in near- and mid-UV. (left) $\lambda = 3000 \text{ \AA}$: the aperture diffraction conceals most of mirror defects, the HEW is not much larger than that of a perfect mirror of the same size (32.4 arcsec, see Fig. 4). (right) $\lambda = 1000 \text{ \AA}$: the diffraction off the aperture ($\Delta R = 1.1 \text{ mm}$) is reduced and the PSF due to mirror shape becomes visible.

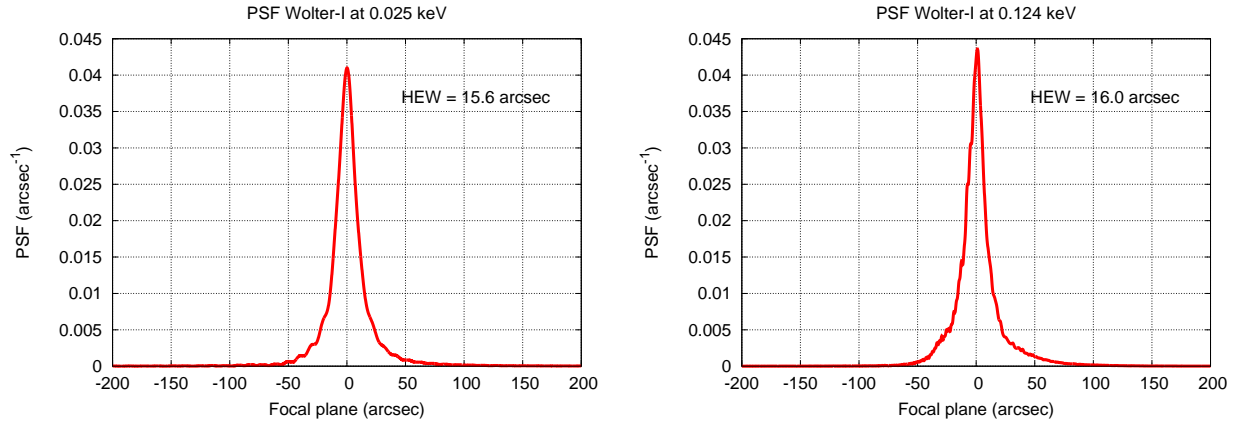


Figure 9. The simulated PSF in far UV. (left) $\lambda = 500 \text{ \AA}$: the PSF is solely determined by mirror shape deviations, and the HEW has decreased to a minimum value. (right) $\lambda = 100 \text{ \AA}$: aperture diffraction fringes have completely disappeared, and the PSF is almost equal to the ray-tracing result from the the sole figure (compare with Fig. 6).

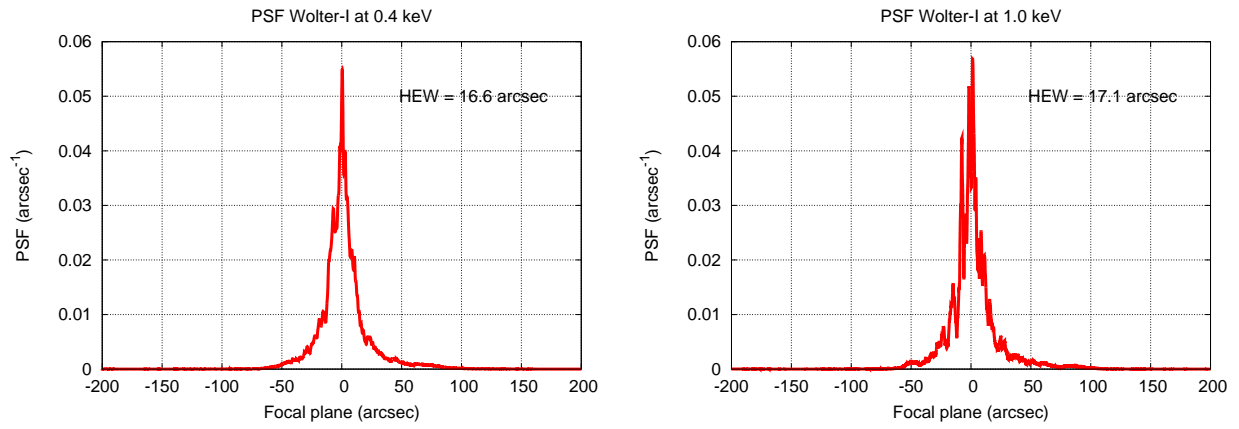


Figure 10. The simulated PSF in soft X-rays. (left) $\lambda = 30 \text{ \AA}$. (right) $\lambda = 12 \text{ \AA}$: the first roughness effects start to appear.

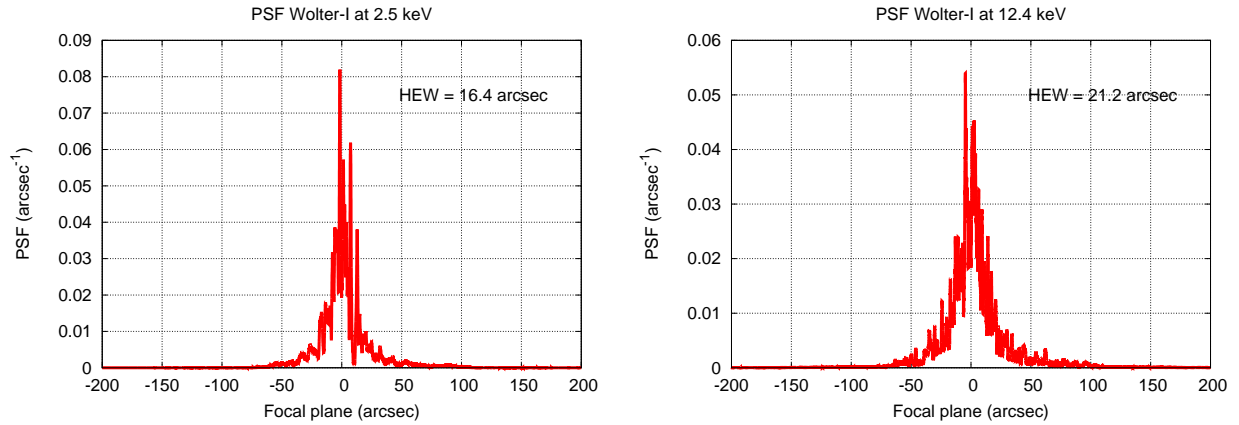


Figure 11. The simulated PSF in soft X-rays. (left) $\lambda = 5 \text{ \AA}$. (right) $\lambda = 1 \text{ \AA}$: the effects of roughness are now clearly seen. The PSF is much broader and the HEW is rapidly increasing.

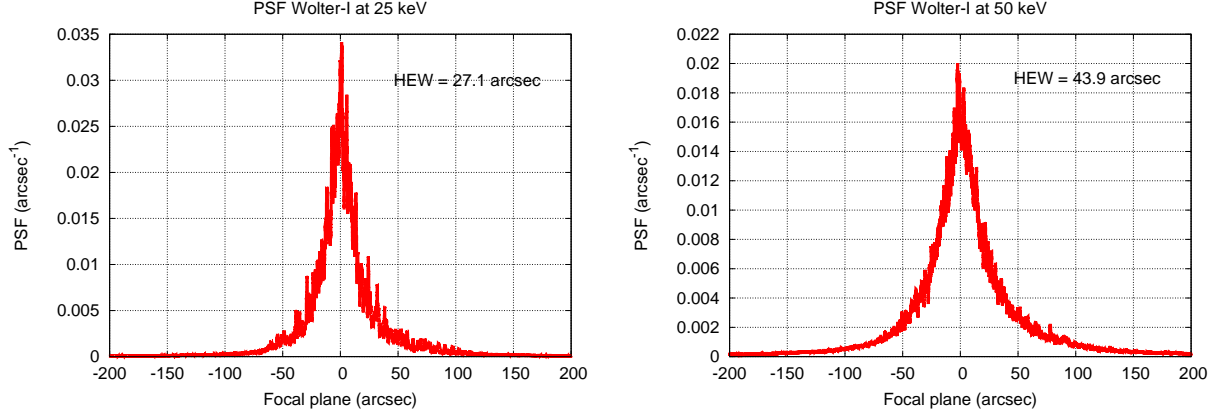


Figure 12. The simulated PSF in hard X-rays. (left) $\lambda = 0.5 \text{ \AA}$. (right) $\lambda = 0.25 \text{ \AA}$: the X-ray scattering is now overwhelmingly dominating.

5. THEORETICAL AND EXPERIMENTAL VALIDATION OF RESULTS

We finally deal with a comparison of results of Sect. 4.4 with the HEW trend directly obtained from the roughness PSD, along with the analytical formalism¹¹ mentioned in Sect. 1. This method, applicable provided that a separation between figure roughness and scattering can be clearly set, allows us deriving the X-ray scattering term of the HEW as a function of λ , $H(\lambda)$, from the roughness PSD. This is the case of the mirror imperfections treated in Sect. 4.4, which are obtained by superimposing a long-period deformation to a microroughness profile: even though the PSD partially overlaps the spectral range of the assumed figure error, the amplitude of rough profile is much smaller (a few angströms Vs. a few microns), hence the mid-frequency component is very low. Moreover, the PSD fulfills the smooth surface limit (Eq. 1) for almost all the energies considered in the computation ($< 55 \text{ keV}$), therefore the XRS theory at the first order can be applied to a good approximation. In the particular case of a power-law PSD²⁰ like the one adopted in Sect. 4.4, $H(\lambda)$ can be written in an explicit and useful form:¹¹

$$H(\lambda) = 2 \left[\frac{16\pi^2 K_n}{(n-1) \ln \gamma} \right]^{\frac{1}{n-1}} \left(\frac{\sin \alpha}{\lambda} \right)^{\frac{3-n}{n-1}}, \quad (19)$$

where $\gamma = 2$ for a single reflection and $\gamma = 4/3$ for the double reflection (Wolter-I) case. The HEW trends for the parameter values used in Sect. 4.4 are reported as lines in Fig. 13 (left), for both single and double reflection cases. The respective HEW values, computed from the PSFs using the Fresnel diffraction applied to the sole roughness profiles, are plotted with symbols in the same graph.

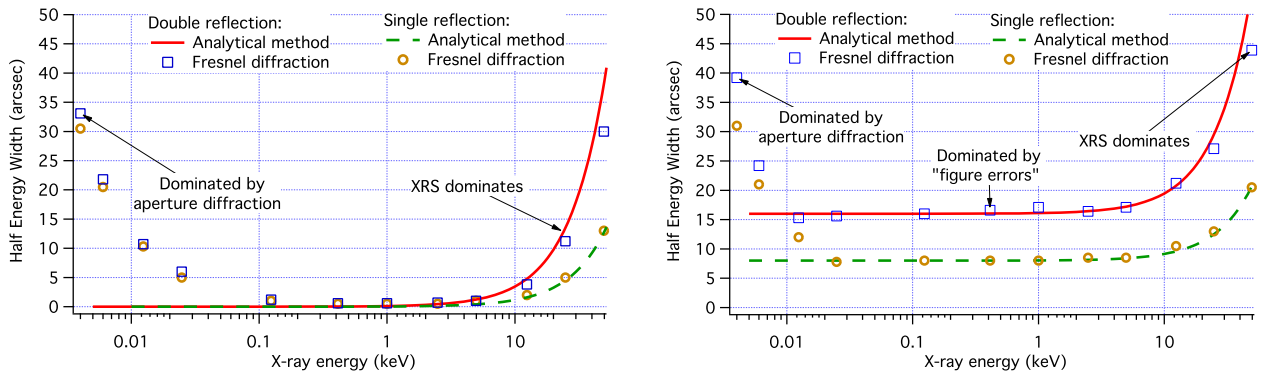


Figure 13. HEW results as computed by means of the analytical method (lines) and using the Fresnel diffraction (symbols). (left) only roughness PSD, (right) roughness and figure errors, same parameters as in Sect. 4.4.

At low energies, the two trends differ because the Fresnel diffraction method also accounts for aperture diffraction, while Eq. 19 does not. At high energies, the HEW computed with the two methods increase in mutual accord: the slight HEW overestimation with the analytical formula at higher energies can be due to the small scattering angles approximation, required by the 1st order XRS theory, which is not exactly fulfilled (the Fresnel diffraction method does not require this condition). The low- and high-energy regimes are separated by a wide plateau where neither the aperture diffraction nor the scattering are relevant. Since no figure errors are by now assumed, the HEW plateau is close to zero.

If the figure error term is added to the rough profile, we obtain the PSF simulated in Figs. 8 through 12. The HEW trend (Fig. 13, right, symbols) appears similar to the one in the left graph, but the mid-energy plateau is at a 8 arcsec HEW for the single reflection and at a 16 arcsec HEW for the Wolter-I case. These figure error HEW values are the same obtained from the computation in Sect. 4.3 using the sole figure errors, taken with the same sign. The analytical simulations match the Fresnel diffraction results, for both single and double reflection, only if the respective figure error HEW values are added *linearly* to the $H(\lambda)$ functions computed from the sole PSD. In other words, *the XRS and the figure error terms of the HEW, when they can be computed separately, are apparently to be combined linearly*¹⁴ and not quadratically as initially supposed.¹¹ This does not disprove the validity of the analytical approach, but it seemingly suggests the correct way to mix the two contributions. Tab. 1 compares the advantages of either method to compute the PSF.

	Fresnel diffraction ¹⁴	Analytical method ¹¹
Computation result	Point Spread Function	Half Energy Width (XRS)
Smooth-surface condition	<i>Not required</i>	Required
Separation figure/roughness	<i>Not required</i>	Required
Mid-frequency treatment	<i>Fully consistent</i>	Uncertain
Computation time	Variable	<i>Very fast</i>
Formalism inversion	Very difficult	<i>Very easy</i>
Aperture diffraction	<i>Included</i>	Not included
Roundness errors	Not included	Not included

Table 1. Performances and drawbacks of the PSF computation based on Fresnel diffraction, and of the analytical method to translate the PSD into an HEW (and vice versa).

An experimental proof in favor of the proposed methods (including the linear sum of figure and XRS) is provided in another paper of this volume,¹⁷ where we report the hard X-ray tests we performed at the SPring-8 synchrotron facility (JASRI, Japan) on an electroformed Wolter-I mirror for the NHXM project.¹⁸ Not only *the measured HEW trend is found to be in agreement with the analytically computed one from the figure and roughness measurement, but also the PSF measured in hard X-rays is very well reproduced by the application of the Fresnel diffraction to the measured mirror profiles and roughness*. This proves not only the accuracy of X-ray measurements and metrological characterizations, but also the correctness of the Fresnel diffraction method as a predictive approach to the PSF computation from mirror metrology.

6. CONCLUSIONS

We have proposed a self-consistent method to compute the PSF of a single- or double-reflection X-ray mirror, based on the Huygens-Fresnel principle. The method does not require distinguishing between figure errors and roughness, between ray-tracing and scattering, and works at all energies, accounting also for aperture diffraction. It also provides a consistent treatment of mid-frequencies. The only approximations needed are that the incidence angle is shallow (i.e., < a few degrees), and that the roundness errors have a negligible impact on the PSF. We have drawn our attention to a widespread category of double-reflection mirrors in X-ray astronomy, the Wolter-I, verifying that the resulting PSF behaves as per the expectations, taking the parameters of a NHXM mirror shell as a test case. The PSF computation reproduces the ray-tracing results wherever the geometrical optics may be applied. In hard X-rays, the single- and double-reflection results are consistent with the prediction of the analytical model, when it is applicable, provided that the separate contributions to the HEW from the geometrical profile and from the microroughness are summed linearly. Finally, the application of the Fresnel

diffraction to the real data out of profile and roughness metrology of a Wolter-I mirror shell for the NHXM optics¹⁸ is in very good agreement with the PSFs measured at the SPring-8 radiation facility.¹⁷ The applications of this method to the development of X-ray optics for astronomy or terrestrial sources are potentially numerous.

ACKNOWLEDGMENTS

This work has been financed by the Italian Space Agency (contract I/069/09/0).

REFERENCES

- [1] L. P. Van Speybroeck & R. C. Chase, "Design parameters of paraboloid-hyperboloid telescopes for X-ray astronomy", *Applied Optics*, 11, 2, 440-445 (1972)
- [2] P. Conconi & S. Campana, "Optimization of grazing incidence mirrors and its application to surveying X-ray telescopes", *Astronomy & Astrophysics*, 372, 1088-1094 (2001)
- [3] P. Conconi, S. Campana, G. Tagliaferri, et al., "A wide field X-ray telescope for astronomical survey purposes: from theory to practice", *Monthly Notices of the Royal Astronomical Society*, 405, 877-886 (2010)
- [4] P. Kirkpatrick & A. V. Baez, "Formation of optical images by x-rays", *JOSA*, 38, 766K (1948)
- [5] P. A. J. De Korte, R. Giralt, J. N. Coste, et al., "EXOSAT X-ray imaging optics", *Applied Optics*, 20, 1080-1088 (1981)
- [6] E. L. Church, H. A. Jenkinson, and J. M. Zavada, "Relationship between surface scattering and microtopographic features", *Optical Engineering*, 18, 125-136 (1979)
- [7] J. C. Stover, "Optical scattering: measurement and analysis", SPIE Optical Engineering Press (1995)
- [8] F. E. Christensen, A. Hornstrup, and H. W. Schnopper, "Surface correlation function analysis of high resolution scattering data from mirrored surfaces obtained using a triple-axis X-ray diffractometer", *Applied Optics*, 27, 1548-1563 (1988)
- [9] R. Willingale, "ROSAT wide field camera mirrors", *Applied Optics*, 27, 1423-1439 (1988)
- [10] S. L. O'Dell, R. F. Elsner, J. J. Kołodziejczak, et al., "X-ray evidence for particulate contamination on the AXAF VETA-1 mirrors", *SPIE Proc.*, 1742, 171-182 (1993)
- [11] D. Spiga, "Analytical evaluation of the X-ray scattering contribution to imaging degradation in grazing-incidence X-ray telescopes", *Astronomy & Astrophysics* 468, 775-784 (2007)
- [12] B. Aschenbach, "Boundary between geometric and wave optical treatment of x-ray mirrors", *SPIE Proc.*, 5900, 59000D (2005)
- [13] J. E. Harvey, E. C. Moran, and W. P. Zmecz, "Transfer function characterization of grazing incidence optical systems", *Applied Optics*, 27, 1527-1533 (1988)
- [14] L. Raimondi & D. Spiga, "Self-consistent computation of X-ray mirror point spread functions from surface profile and roughness", *SPIE Proc.*, Vol. 7732, 77322Q (2010)
- [15] P. Zhao & L. P. Van Speybroeck, "New method to model X-ray scattering from random rough surfaces", *SPIE Proc.*, 4851, 124-139 (2003)
- [16] A. L. Mieremet, M. W. Beijersbergen, "Fundamental spatial resolution of an x-ray pore optic", *Applied Optics*, 44(33), 7098-7105 (2005)
- [17] D. Spiga, L. Raimondi, A. Furuzawa, et al., "Angular resolution measurements at SPring-8 of a hard X-ray optic for the New Hard X-ray Mission", *SPIE Proc.* 8147, this conference (2011)
- [18] S. Basso, G. Pareschi, O. Citterio, et al., "The optic system of the New Hard X-ray Mission: status report", *SPIE Proc.* 8147, this conference (2011)
- [19] A. Moretti, S. Campana, G. Tagliaferri, et al., "SWIFT XRT Point Spread Function measured at the Panter end-to-end test", *SPIE Proc.* 5165, 232-240 (2004)
- [20] E. L. Church, "Fractal Surface finish". *Applied Optics*, 27(8), 1518 -1526 (1988)